Experiments in Fluids 28 (2000) 322–335 © Springer-Verlag 2000

Whole-field density measurements by 'synthetic schlieren'

S. B. Dalziel, G. O. Hughes, B. R. Sutherland

Abstract This paper outlines novel techniques for producing qualitative visualisations of density fluctuations and for obtaining quantitative whole-field density measurements in two-dimensional density-stratified flows. These techniques, which utilise image processing technology, are much simpler to set up than the classical schlieren and interferometry methods, and provide useful information in situations where shadowgraph is of little or no value. Moreover, they may be set-up to analyse much larger domains than is feasible with the classical approaches, and do not require high quality optical windows in the experimental apparatus. Ultimately the greatest strength of these techniques is the ability to extract accurate, quantitative measurements of the density field.

Application of these techniques is illustrated by an internal wave field produced by an oscillating cylinder. Recent theoretical advances for this classical problem make it the ideal test bed. Results are presented for both a circular and a square cylinder oscillating vertically in a linear stratification. Further aspects of the techniques are illustrated by considering thermal convection from a hand and flow over an obstacle towed through a density stratified fluid.

Received: 27 October 1998 /Accepted: 24 May 1999

S. B. Dalziel, G. O. Hughes[1], B. R. Sutherland[2]
Department of Applied Mathematics and Theoretical Physics
The University of Cambridge, Silver Street
Cambridge CB3 9EW, England

Present addresses:
[1] Research School of Earth Sciences, The Australian National University, Canberra, A.C.T. 0200, Australia
[2] Department of Mathematical Sciences, University of Alberta, Edmonton, Alberta T6G 2G1, Canada

Correspondence to: S. B. Dalziel

SBD wishes to acknowledge the support of AWE, Yorkshire Water and the Isaac Newton Trust. GOH thanks the Association of Commonwealth Universities for his time in DAMTP and acknowledges the support of NERC under grant GR3/9356 for the experiments conducted in the EnFlo towing-tank. BRS acknowledges support from NERC under grant GR3/09399. The authors also wish to thank an anonymous reviewer for drawing our attention to early work on the Moiré fringe methods in the 1940s and 1950s.

1
Introduction

Qualitative visualisations of density fluctuations have long been used to assist with the understanding of flows in density stratified systems. The techniques range from the introduction of passive tracers, such as dye lines or neutrally buoyant particles, to shadowgraph, schlieren and interferometric techniques which rely on refractive index variations induced by the stratifying agent. Numerous examples of these visualisations may be found within the literature (e.g. van Dyke 1982), as have attempts to extract quantitative information from them (e.g. Irvin and Ross 1991; Greenberg et al. 1995).

In this paper we introduce a number of novel techniques for obtaining both high quality visualisations and accurate measurements of the density field. These techniques are based on the same optical principles as the classical schlieren method, but have the advantages of being much easier to set-up and of being adaptable to much larger domains. The name which has been chosen for the simplest of these techniques – 'qualitative synthetic schlieren' – reflects the relationship with classical schlieren, although we note that it is the optics (external to the flow) used to form the schlieren image which are "synthesised", not the optical inhomogeneities of the medium being visualised. The most sophisticated of the quantitative techniques has been named 'pattern matching refractometry' to indicate the origin of the approach in 'pattern matching velocimetry' (more frequently called 'particle image velocimetry').

In total we shall outline four techniques: 'qualitative synthetic schlieren', 'line refractometry', 'dot tracking refractometry' and 'pattern matching refractometry'. The first of these has two modes of operation, 'line mode' and 'dot mode' and these represent the basic qualitative visualisation behind the remaining three quantitative techniques. For this reason we often refer to all four techniques as 'synthetic schlieren'. These techniques are primarily of value for analysing two-dimensional flows where the curvature of the density field is sufficiently small that classical shadowgraph techniques are of limited value, although there is an overlap in the range of applicability. They may also be used for flows where the density gradients are too small for techniques relying on the concentration of a passive dye (e.g. light induced fluorescence or dye absorption) to give useful results. While limited information can be extracted from flows with three-dimensional variations in the density field, we shall not discuss these in any detail.

This paper is intended to complement and expand on the subset of these techniques presented by Sutherland et al. (1999) in their analysis of the internal wave field in stratified salt water solutions produced by an oscillating cylinder, and to provide more detail than may be found in Dalziel et al. (1998). We again employ internal wave fields as our primary method of illustrating the techniques. It is therefore appropriate to review some aspects of flow in a density-stratified fluid, although the intention here is to illustrate the power of synthetic schlieren rather than present a detailed analysis of the fluid dynamics.

If a fluid element is perturbed vertically in a density stratified fluid, it experiences a buoyancy force directed to restore it to its original position. This buoyancy force, in combination with the inertia of the fluid element, act as a simple harmonic oscillator with a frequency (the buoyancy frequency)

$$N = \left(-\frac{g}{\rho_0}\frac{\partial\rho}{\partial z}\right)^{1/2} \ , \tag{1}$$

where ρ is the fluid density with reference density ρ_0, g is gravity and z is oriented vertically upward. Oscillation in a direction at an angle θ to the vertical reduces the restoring force, giving rise to the dispersion relation for small amplitude waves in a Boussinesq fluid,

$$\omega = \pm N \cos\theta \ , \tag{2}$$

where ω is the frequency of the waves. The fluid motion and group velocity are at an angle θ to the vertical, while the phase velocity is perpendicular to this (the sign of the vertical component of the phase velocity is opposite to that of the group velocity).

A linearly stratified fluid ($N = \text{const}$) is therefore able to support waves of frequencies $0 \leq \omega \leq N$. Mowbray and Rarity (1967) demonstrated theoretically and experimentally (using classical schlieren) that for waves forced by an oscillating cylinder, the fluid motion was confined with a region of fluid resembling a "St. Andrew's Cross". This is in sharp contrast to the flow found when the fluid is unstratified (e.g. Lin and Rockwell 1997 who looked at the vortex shedding from an oscillating cylinder). Other authors have subsequently used different experimental techniques to analyse these waves (e.g. Peters 1985 and Merzkirch and Peters 1992 used interferometry). Recent work by Hurley and Keady (1997) has provided additional theoretical details of the structure of this wave field for cylinders of a finite size in a viscous fluid, The first experimental results confirming their prediction are provided by Sutherland et al. (1999). In the experiments presented here a circular cylinder of radius $R = 20$ mm is oscillated vertically in a linear stratification with $N \sim 1\ \text{s}^{-1}$ and $\omega/N \sim 2^{-1/2}$.

Internal waves are also generated if an obstacle is towed horizontally through a stratification. For a flow which is steady in the frame of reference of the obstacle, the horizontal component of the phase velocity is equal to the speed of towing U, giving rise to waves of frequency $\omega = 2\pi\lambda/U$, where λ is the length scale associated with the object. The need to transport energy away from the obstacle combined with the dispersion relation give rise to an asymmetric pattern of waves with the crests tilted upstream (see Turner 1973; Gill 1982).

After reviewing the basic optics in Sect. 2, we outline the experimental set-up used for the classical schlieren and Moiré fringe methods in Sect. 3. In Sect. 4 the qualitative mode of synthetic schlieren is introduced and Sects. 5–7 discuss the quantitative modes. Finally, Sect. 8 presents our conclusions.

2
Basic optics

All four techniques introduced in this paper utilise the same optical phenomenon, namely that a ray of light is bent towards regions of larger refractive index. A detailed description of this process is required in order to make quantitative measurements. This description may start from a number of points. Sutherland et al. (1999) analysed a ray of light by invoking Snell's law. Here we shall start from Fermat's variational principle for the behaviour of light in an inhomogeneous medium

$$\delta \int n(x,y,z)\mathrm{d}s = 0 \ , \tag{3}$$

where s is oriented along the light ray and $n(x,y,z)$ is the refractive index field (the ratio of the speed of light through a vacuum to that through the medium). We select our coordinate system (x,y,z) with x along the length of the tank, y across the width (the direction in which variations in the flow are negligible) and z vertically upward.

Rather than solving the full variational problem, we restrict ourselves to rays of light which always have a component in the y direction so that their paths may be described by $x = \xi(y)$ and $z = \zeta(y)$. This restriction is simply a requirement that light is able to cross the tank, a fundamental requirement for the methods described in this paper. The variational principle then gives rise to a pair of coupled ordinary differential equations (Weyl 1954) relating the light path to the gradients of n in the x-z plane:

$$\frac{\mathrm{d}^2\xi}{\mathrm{d}y^2} = \left[1 + \left(\frac{\mathrm{d}\xi}{\mathrm{d}y}\right)^2 + \left(\frac{\mathrm{d}\zeta}{\mathrm{d}y}\right)^2\right]\frac{1}{n}\frac{\partial n}{\partial x} \ , \tag{4a}$$

$$\frac{\mathrm{d}^2\zeta}{\mathrm{d}y^2} = \left[1 + \left(\frac{\mathrm{d}\xi}{\mathrm{d}y}\right)^2 + \left(\frac{\mathrm{d}\zeta}{\mathrm{d}y}\right)^2\right]\frac{1}{n}\frac{\partial n}{\partial z} \ . \tag{4b}$$

For synthetic schlieren we are interested primarily in light rays which remain approximately parallel to the y direction. Under this restriction the terms $(\mathrm{d}\xi/\mathrm{d}y)^2$ and $(\mathrm{d}\zeta/\mathrm{d}y)^2$ may be neglected, effectively decoupling (4a) and (4b). The two-dimensionality of the flow and the weak variations in density (and hence weak variations in the refractive index) along the ray path allow these expressions to be integrated across the width W of the tank to obtain the path of the light ray across the tank:

$$\xi = \xi_i + y\tan\phi_\xi - \frac{1}{2}y^2\frac{1}{n}\frac{\partial n}{\partial x} \ , \tag{5a}$$

$$\zeta = \zeta_i + y\tan\phi_\zeta - \frac{1}{2}y^2\frac{1}{n}\frac{\partial n}{\partial z} \ , \tag{5b}$$

where ξ_i, ζ_i describe the incident location and $\tan\phi_\xi = \mathrm{d}\xi/\mathrm{d}y(y=y_0)$ and $\tan\phi_\zeta = \mathrm{d}\zeta/\mathrm{d}y(y=y_0)$ describe the horizontal and vertical components (respectively) of the angle at which the light ray enters the tank (measured relative to the y direction).

As shall be seen in the following sections, we are interested in how an image of a mask placed some distance B behind the tank (the reason for choosing $B \neq 0$ will be given in Sect. 4) appears to change as the result of flow-induced refractive index variations relative to the refractive index variations in the absence of the flow. Specifically we wish to analyse the changes in the image formed by the camera as a shift in the origin of the light ray reaching the camera. By back-tracing the light rays received by the camera the apparent shift $(\Delta\xi, \Delta\zeta)$ in the origin of the light ray is given by

$$\Delta\xi = \frac{1}{2}W(W+2B)\frac{1}{n_0}\frac{\partial n'}{\partial x} \quad , \tag{6a}$$

$$\Delta\zeta = \frac{1}{2}W(W+2B)\frac{1}{n_0}\frac{\partial n'}{\partial z} \quad . \tag{6b}$$

Here we have decomposed the refractive index field n into $n_0 + n_{\mathrm{base}} + n'$ where n_0 is the nominal refractive index of the medium (e.g. $n_0 = 1.3332$ for water), n_{base} represents spatial variations associated with the "known" base state (e.g. the changes introduced by adding a quiescent linear background stratification) and n' is the variation caused by the flow under consideration (e.g. the internal wave field). In obtaining (6) we have assumed the variations n_{base} and n' in the refractive index field are small compared with nominal value n_0.

In principle there should be some correction made to (6) for the refractive index contrasts between air, the material the tank is made of and the working fluid. Details of this correction, using Snell's law, are presented in Sutherland et al. (1999). In practice, however, provided the incident light rays are approximately normal to the tank walls (which is the requirement to ignore the $(\mathrm{d}/\mathrm{d}y)^2$ terms in (5)) the additional refraction at these optical interfaces need not be considered explicitly.

As stated above, there is normally a constitutive relationship between the density of the fluid and the refractive index. To a good approximation the relationship between refractive index and density for salt water is linear (Weast 1981), allowing us to write

$$\nabla n = \frac{\mathrm{d}n}{\mathrm{d}\rho}\nabla\rho = \beta\frac{n_0}{\rho_0}\nabla\rho \quad , \tag{7}$$

where

$$\beta = \frac{\rho_0}{n_0}\frac{\mathrm{d}n}{\mathrm{d}\rho} \approx 0.184 \quad , \tag{8}$$

and ρ_0 is the nominal reference density ($1000\,\mathrm{kg\,m^{-3}}$). Substitution into (6) then gives the relationship between density fluctuations ρ' and apparent movement of the source of a light ray

$$\Delta\xi = \frac{1}{2}W(W+2B)\frac{\beta}{\rho_0}\frac{\partial\rho'}{\partial x} \quad , \tag{9a}$$

$$\Delta\zeta = \frac{1}{2}W(W+2B)\frac{\beta}{\rho_0}\frac{\partial\rho'}{\partial z} \quad . \tag{9b}$$

3
Schlieren and Moiré fringes

The classical schlieren method makes use of the deflection of a ray of light to mask off a greater or lesser portion of the light source with the edge of a "knife". Figure 1 illustrates a typical set-up. The light source in combination with the first parabolic mirror produces a field of nominally parallel light rays. As these light rays pass through the tank they are bent towards the gradient of the refractive index, and hence density. If the basic state is represented by a linear stratification then (5) shows the light rays will execute a parabolic mirror which projects an image onto a screen via a lens.

The knife edge is positioned near the focal point of the second parabolic mirror and lens, and acts as an asymmetric aperture. Typically it is adjusted so that half of the light passing through the tank with quiescent conditions is obscured by the knife edge. When the flow produces refractive index variations n', the light rays leaving the tank are deflected so that the mirror no longer focuses them at the knife edge. Depending on the direction of this deflection and the orientation of the knife edge, the amount of light striking the knife may be increased (decreased), leading to a reduction (intensification) of the light reaching the corresponding position on the screen. The orientation of the knife edge in Fig. 1 is chosen so that the intensity of the image increases with positive $\partial\rho'/\partial\uparrow$. The symbol $\uparrow$ is used here to represent the deflection direction corresponding to the normal to the knife edge (e.g. upward for the arrangement shown in Fig. 1).

There are a number of practical difficulties with this classical schlieren. First, the setting up of the optical components, especially the parabolic mirrors, requires considerable care. Second the cost of parabolic mirrors

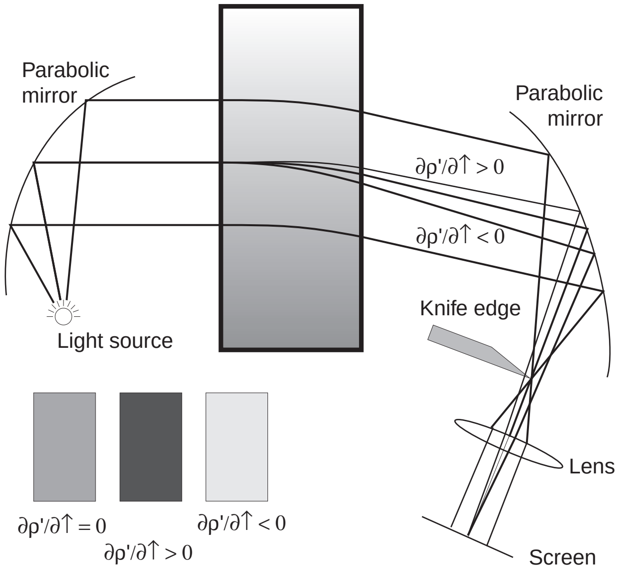

Fig. 1. Sketch of optical arrangement for classical schlieren method

rapidly becomes prohibitive with increasing size. Third, high quality images can only be formed when the apparatus itself is optically good (e.g. optical quality glass rather than Perspex which is prone to scratching), adding further to the cost. Moreover, if the base state described by n_{base} is not itself either constant or linear, then the unperturbed light rays are not parallel, yielding an unwanted structure in the image formed for this base state. Finally, the need for a point source of illumination limits the intensity of illumination available.

Using the knife edge illustrated in Fig. 1 it is possible to visualise only the component of $\nabla\rho'$ normal to the edge. To overcome this a number of techniques have used different geometries to mask the focal point in place of a knife edge, as have methods for obtaining quantitative information from the resulting images through accurate determination of the intensity of the image (e.g. Irvin and Ross 1991) or determining the colour produced by a colour schlieren system (e.g. Greenberg et al. 1995).

The Moiré fringe method (e.g. Burton 1949; Mortensen 1950; Sakai 1990) represents an optically simpler alternative to the classical schlieren. Two masks of alternating clear and opaque lines (or dots), with a spacing greater than the diffraction limit, are produced with one being positioned on either side of the flow. Diffuse lighting illuminates the mask behind the tank. The mask in front of the tank is positioned and scaled in such a way that, for a fixed observer and no perturbations to the flow the masks appear to have the same line spacing. When the flow is initiated the density field is perturbed and the light rays reaching the observer originate from a different location on the mask behind the tank. This location may result in either more or less light reaching the observer depending on the magnitude and direction of $\nabla\rho'$ and the phase relationship between the two masks. Such a situation is illustrated in Fig. 2 where the phasing of the lines on the two masks has been selected so as to increase the mean intensity (averaged over a region larger than the line spacing) for positive $\partial\rho'/\partial\uparrow$ (here $\uparrow$ represents the direction perpendicular to the lines). If there had been no phase difference between the two sets of lines then the image would have got darker for either sign of $\partial\rho'/\partial\uparrow$, while a 180° phase difference would have started from a black image and got brighter for $|\partial\rho'/\partial\uparrow| > 0$.

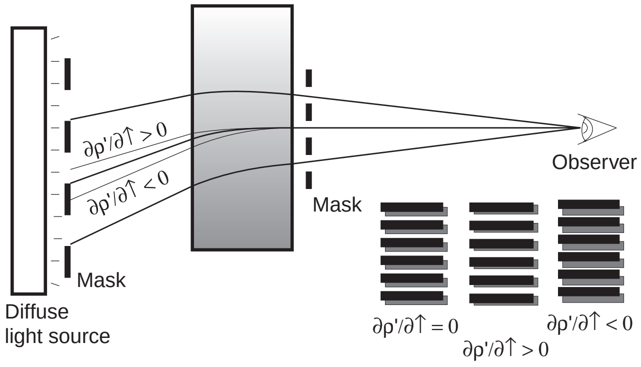

Fig. 2. Sketch of optical arrangement for Sakai's Moiré method

There are a number of experimental difficulties with this Moiré fringe arrangement. The production of suitable masks is relatively straight forward using modern laser printers, provided the geometry of the masks is related by a simple scalar. Their positioning, however, is fairly critical as accurate alignment of both masks and the observer is necessary. Achieving the required level of alignment for a stratified flow may require the mask nearer the observer to have a non-uniform line spacing, even when the mask behind the tank is uniform. Moreover, the precise positioning of the mask and spacing of the lines will depend on the background stratification. A decrease in the buoyancy frequency of this background stratification, for example, will require the mask located in front of the tank to be positioned higher than that required when the stratification is stronger, while a nonlinear stratification will require a nonlinear relationship between the lines on the two masks.

The optical arrangement illustrated in Fig. 2 is not the only one which may be used. Replacing the observer with a point light source and the diffuse light source with a projection screen will yield an equivalent result by tracing in the reverse direction along the light rays. This duality leads to an alternative method of generating the larger of the two masks. The geometry of this larger mask, located further from the light source, may be determined by simply projecting the smaller mask through the tank (when it contains the ambient stratification) onto the location of the second (larger) mask. The required geometry may then be recorded in situ by positioning photographic film in place of the mask. After developing, this photographic film may be used as the mask. Any phase difference required between the two masks can be achieved by applying a suitable translation to the regular geometry of the smaller mask prior to exposing the film.

If carefully set-up, the Moiré fringe method is capable of producing high quality visualisation with excellent spatial resolution at only a small fraction of the cost for conventional schlieren. However, as we will see in the next section, synthetic schlieren avoids most of the difficulties with setting up the Moiré fringe method.

4

Qualitative synthetic schlieren

The photographic production of one of the masks for the Moiré fringe method outlined in the previous section forms the basis of the qualitative synthetic schlieren methods introduced in this section. The fundamental idea is to record digitally (rather than photographically) the apparent location of one of the masks. The image recorded in this way then forms a virtual mask against which the apparent movements due to refractive index gradients may be measured. This approach works in both the diffuse light source (such as shown in Fig. 3) and point light source arrangements. In either case the real mask is placed between the light source and the tank, while the virtual mask is created from the appearance of the real mask in the absence of perturbations to the quiescent state. The main restriction is that the depth of field of the video camera (or light source if projecting the mask through the tank) is large enough such that both the flow and the mask are

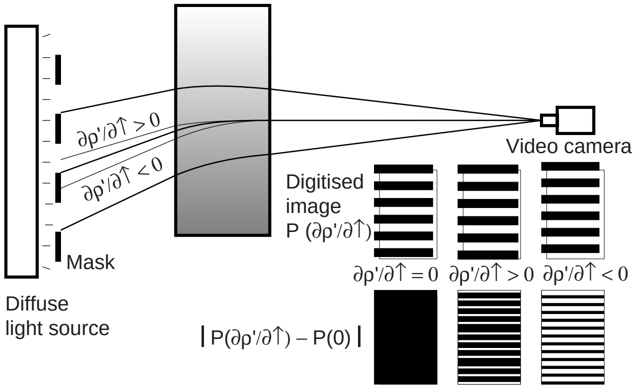

Fig. 3. Sketch of optical arrangement for line-mode synthetic schlieren

reasonably well in focus so that we may identify the light falling on a pixel in the video camera with a single ray passing through the tank. This is not a severe restriction as the experimental arrangement allows for high levels of illumination to be used (unlike classical schlieren, there is no need for the illumination to originate from a point source), and hence small lens apertures do not cause difficulties.

We shall start by considering a mask with lines parallel to the x direction. With such a set of lines we will be able to visualise $\partial\rho'/\partial z$ through the vertical deflection of the lines (9b), but the uniformity of the basic mask in the x direction makes the visualisation insensitive to $\partial\rho'/\partial x$.

4.1
Basic operation

Figure 4a sketches the typical appearance of the mask for quiescent conditions and with density perturbations resulting in an apparent shift. For the present we shall assume the optics are perfect (this assumption will be relaxed in subsequent sections) and an image of the mask is formed on the surface of the image sensor in the video camera. For a typical video camera operating in frame integration mode the CCD sensor consists of an array of almost touching rectangular pixels, each of which returns a signal $P_{ij}(t)$ proportional to the spatial average of the light intensity striking the ijth pixel:

$$P_{ij}(t) = \frac{1}{\Delta x \Delta z} \int_{x_i-\Delta x/2}^{x_i+\Delta x/2} \left[\int_{x_j-\Delta z/2}^{x_j+\Delta z/2} p(x,z;t)\mathrm{d}z \right] \mathrm{d}x \ . \qquad (10)$$

Here the intensity striking the CCD sensor is $p(x,z;t)$ and the pixel images a region of the mask of size $\Delta x \times \Delta z$. The effect of this averaging or pixelisation is illustrated in Fig. 4b.

For simplicity we will start by assuming that sharp transitions in intensity in the mask produce identically sharp transitions in the intensity $p(x,z;t)$ falling on the CCD sensor. Consider a mask consisting of nominally horizontal lines oriented parallel to the x axis. If the lines are perfectly black ($p = 0$) and perfectly white ($p = 1$) then

$$p_0(x,z) = \begin{cases} 0 & 0 \le z \bmod \eta < \alpha \\ 1 & \text{otherwise} \end{cases} \qquad (11)$$

represents the intensity produced by the mask under quiescent conditions. Here η is the spacing of the lines on the mask and the lines consist of alternating black and white regions of widths $\alpha\eta$ and $(1-\alpha)\eta$, respectively. The intensity of the corresponding digitised image will be

$$P_{ij;0} = \begin{cases} 0 & \frac{1}{2}\Delta z \le z_j \bmod \eta < \alpha\eta - \frac{1}{2}\Delta z \\ 1 & \alpha\eta + \frac{1}{2}\Delta z \le z_j \bmod \eta < \eta - \frac{1}{2}\Delta z \\ \frac{1}{2} + \frac{z_j \bmod \eta - \alpha\eta}{\Delta z} & \alpha\eta - \frac{1}{2}\Delta z \le z_j \bmod \eta < \alpha\eta + \frac{1}{2}\Delta z \\ \frac{1}{2} - \frac{z_j \bmod \eta - \eta}{\Delta z} & \eta - \frac{1}{2}\Delta z \le z_j \bmod \eta < \frac{1}{2}\Delta z \end{cases} . \qquad (12)$$

An expression similar to (12) holds when the density field is perturbed. Provided the perturbations are small such that $\Delta\zeta \le \eta$, where $\Delta\zeta$ is given by (9b), and variations in $\Delta\zeta$ occur over a length scale large compared with η, then we may replace η in (12) with $\eta - \Delta\zeta$. Qualitative mode synthetic schlieren works by calculating $|P_{ij}(t) - P_{ij;0}|$, this difference simply being $|\Delta\zeta|/\Delta z$ and is proportional to $|\partial\rho'/\partial z|$ for pixels which contain an edge in both the $P_{ij;0}$ and $P_{ij}(t)$ images. The constant of proportionality depends on the width of the tank, the relative positions of the mask and the screen, giving

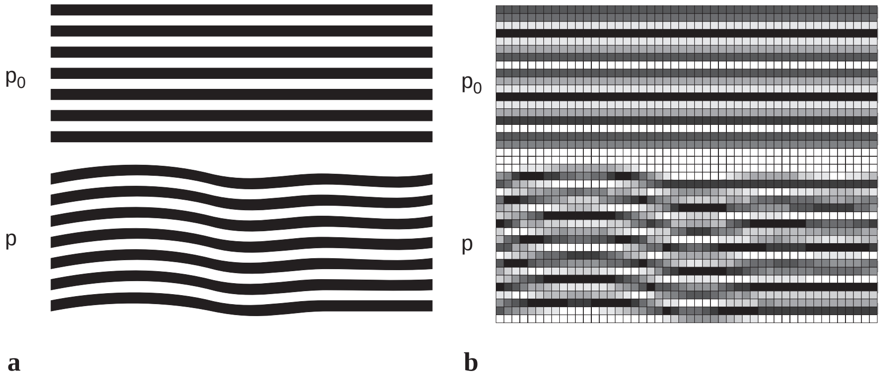

Fig. 4. Idealised images for qualitative synthetic schlieren. **a** Location of lines; **b** image formed in CCD sensor

$$\left|\frac{\partial\rho'}{\partial z}\right|_{ij} = 2\frac{\rho_0}{\beta}\frac{\Delta z}{W(W+2B)} \times \begin{cases} \left|P_{ij}(t) - P_{ij;0}\right| & \text{for pixels containing an edge} \\ \text{unknown} & \text{elsewhere} \end{cases} . \tag{13}$$

In practice the equipment used in this study comprised a standard video camera (Cohu 4910 series set to frame integration mode and no gamma correction) producing an analogue signal which was subsequently digitised to a different horizontal resolution by a frame grabber card (Data Translation DT2862). While this combination makes the situation somewhat more complex than the ideal case described above, the qualitative effect is much the same and $|P_{ij}(t) - P_{ij;0}|$ is proportional to the vertical (for horizontal lines) gradient in the perturbation density.

Figure 5a shows an example of the St. Andrew's cross internal wave field from an oscillating cylinder in a linear density-stratification ($\omega/N \sim 2^{-1/2}$, $N \sim 1\ \text{s}^{-1}$) obtained in this manner. For maximum sensitivity and spatial resolution we would have exactly one line of the mask for every two rows of pixels on the CCD sensor. In practice, however, the spacing and alignment may not be this precise so that the average line spacing exceeds this ideal. As a result the images formed from $|P_{ij}(t) - P_{ij;0}|$ contain striations where there is no data, corresponding to pixels not containing the edge of a line. The sensitivity of this technique is illustrated in Fig. 5b which shows thermal convection in air driven by the heat of a hand. The ambient temperature was 26 °C and the hand surface temperature was only marginally above this.

4.2
Sensitivity

From (13) we can see that the sensitivity may be controlled by the position of the mask relative to the density fluctuations in the flow. Increasing the distance from the object to the mask B increases the sensitivity, although it is necessary to account also for the apparent reduction in the size of the mask (and hence the increase in Δz) as the mask is moved further from the camera. If we assume the unperturbed light rays are straight (thus ignoring the apparent foreshortening due to refractive index changes encountered along the way), we may calculate the relative sensitivity S as the ratio of the apparent deflection of a mask at some distance B behind the tank to that with $B = 0$:

$$S = \frac{L}{L+B}\left(1 + 2\frac{B}{W}\right) = 1 + \frac{B}{W}\frac{L+W}{L+B} . \tag{14}$$

Here we assume the distance between the camera and front wall of the tank is fixed at $L - W$, and the camera zoom remains fixed so that the same region of the tank is visualised for all B. Note that as B is increased, the size of Δz is increased as $L/(L+B)$ compared with $B = 0$.

The sensitivity to thermal convection illustrated in Fig. 5b illustrates one of the difficulties associated with these synthetic schlieren methods, namely the sensitivity to thermal noise in the laboratory environment. For a fixed field of view and distance $L + B$ from the mask, (13) shows that the optical system is most sensitive to thermal noise close to the camera, the sensitivity being proportional to the distance between the thermal anomaly and the mask. It is thus important to minimise the thermal noise, especially close to the camera. Fortunately thermal noise usually evolves on a timescale either much faster or much slower than that for the flow being considered, facilitating its removal through a temporal filtering process, although we will not go into details here.

By setting up the mask on an accurate traverse (the bed of a milling machine equipped with a digital readout with a resolution of approximately ±0.010 mm on relative displacements) we have assessed the sensitivity of the technique without taking any special precautions against

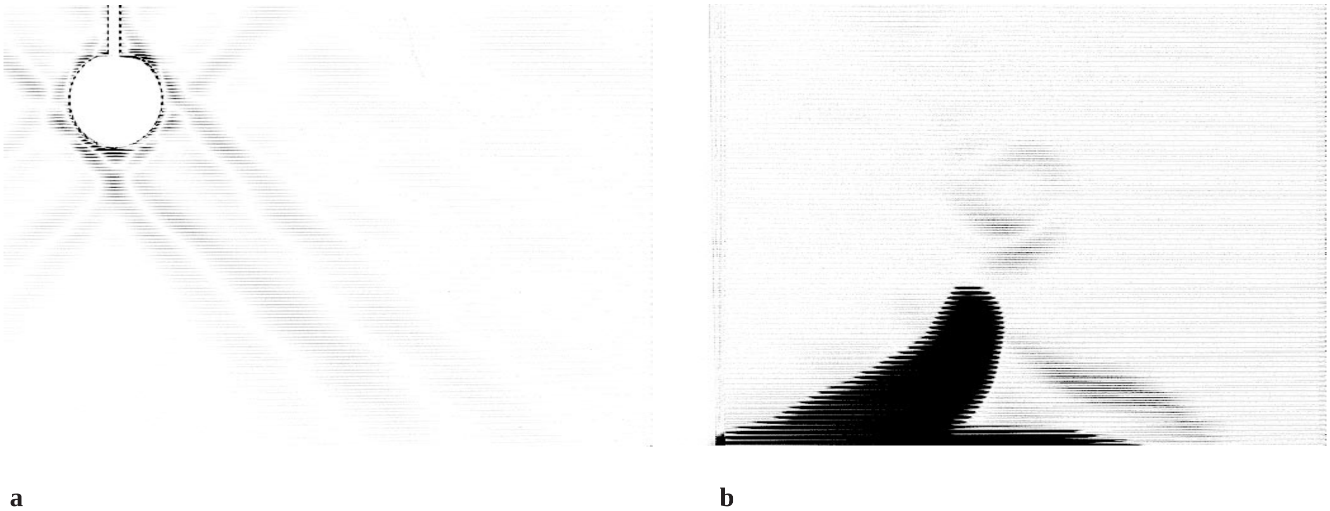

Fig. 5. Line mode qualitative synthetic schlieren. White represents no difference between $P_{ij}(t)$ and $P_{ij;0}$. **a** Internal wave field produced in a linear salt stratification (described by a buoyancy frequency $N \approx 1\ \text{s}^{-1}$) by oscillating a circular cylinder 20 mm in radius at a frequency $\omega \approx N/\sqrt{2}$. **b** Thermal convection from a hand

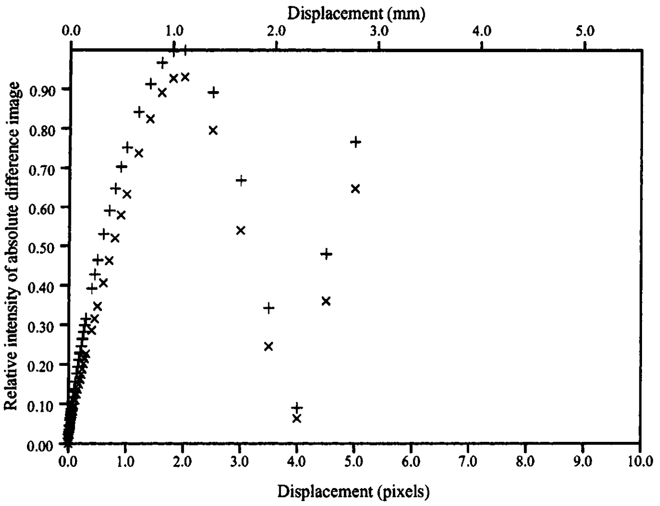

Fig. 6. Variations in the mean (+) and root mean square (×) value of $|P_{ij}(t) - P_{ij;0}|$ as the mask is displaced by a milling machine traverse for a mask of lines aligned with the scan lines of the video camera. The mask was traversed normal to the scan lines of the video camera

thermal noise. Figure 6 shows how the mean level of $|P_{ij}(t) - P_{ij;0}|$ changes with the displacement of the mask of lines. From this we see that displacements as small as 0.01 pixels may be detected with the expected linear response for displacements up to 1 pixel and only a slight departure from linearity for displacements up to 2 pixels. The reduction in $|P_{ij}(t) - P_{ij;0}|$ for larger displacements is the result of aliasing of adjacent lines which have a spacing of a little over 4 pixels. For this test the mask was aligned as closely as possible with the lines parallel to the scan of the standard frame integration video camera used for all the results presented in this paper. The mask was viewed through a zoom lens set to a focal length of 50 mm to image a region 420 mm across. The output of this camera was digitised directly at a resolution of 512 × 512 pixels. We note, in passing, that the thermal environment in the workshop where these tests were undertaken was significantly quieter than in the laboratory.

4.3
Variations on a theme

The above analysis was based on a mask consisting of horizontal lines which are sensitive to fluctuations in the vertical gradient of density. Clearly this is not the only configuration possible. The use of vertical lines yields a measure of the fluctuations in the horizontal gradient, or a pattern of dots yields both components of the gradient. Figure 7a shows the same internal wave field obtained from a regular array of dots, while Fig. 7b illustrates the same for a random array of dots (produced by introducing a random perturbation to a regular array). Careful inspection of either of these reveals information about the direction of the gradient vector in addition to $|\nabla\rho'|$. Figure 7c illustrates this directional information with an enlarged view of the image presented in Fig. 7a. The double-crescent shape is oriented with the gradient directed from one crescent to the other.

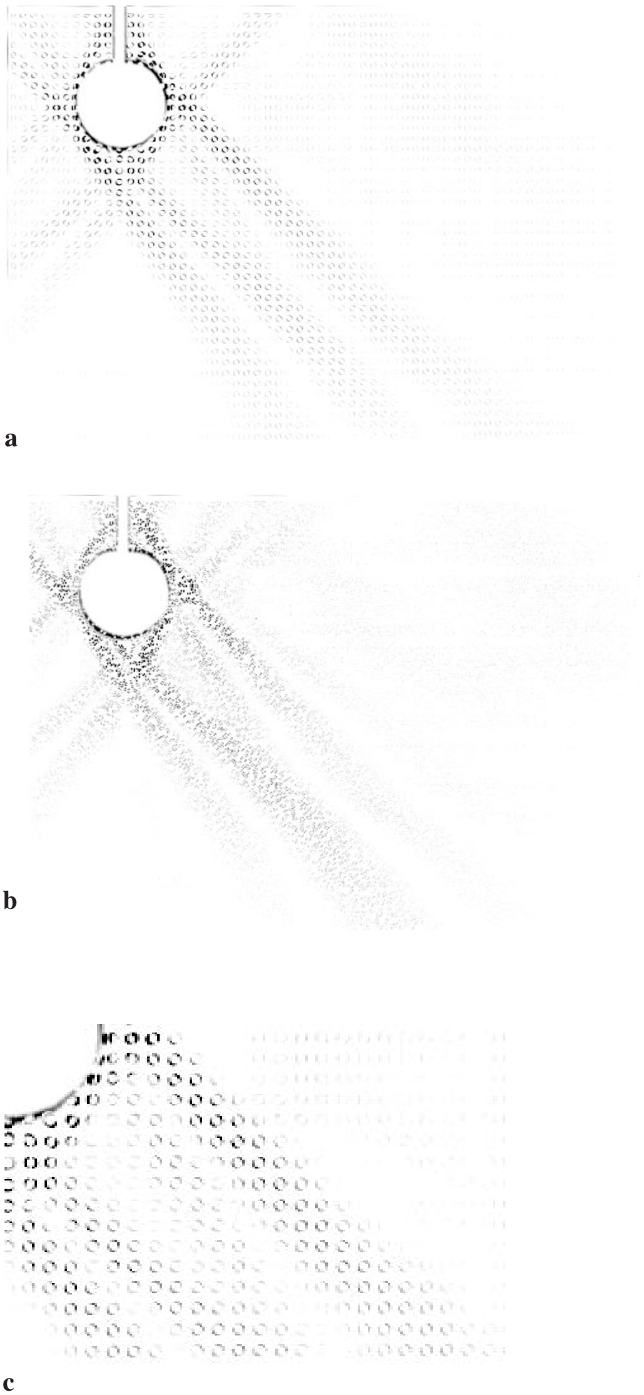

Fig. 7. Qualitative synthetic schlieren using a mask of two-dimensional objects to visualise the internal wave field shown in figure 5. The mask geometries are **a** a regular array of dots and **b** a random array of dots. An enlarged view of the regular array image is shown in **c**

The sensitivity study outlined in Sect. 4.2 for the horizontal lines was repeated for the two mask geometries used for Fig. 7. The corresponding displacement versus $|P_{ij}(t) - P_{ij;0}|$ curves are shown in Fig. 8. We again observe a linear response for displacements less than 1 pixel. For the regular array of dots used for Fig. 8a, we see an aliasing of the (imperfectly aligned) dots for larger displacements, while for the random dots used for Fig. 8b the image

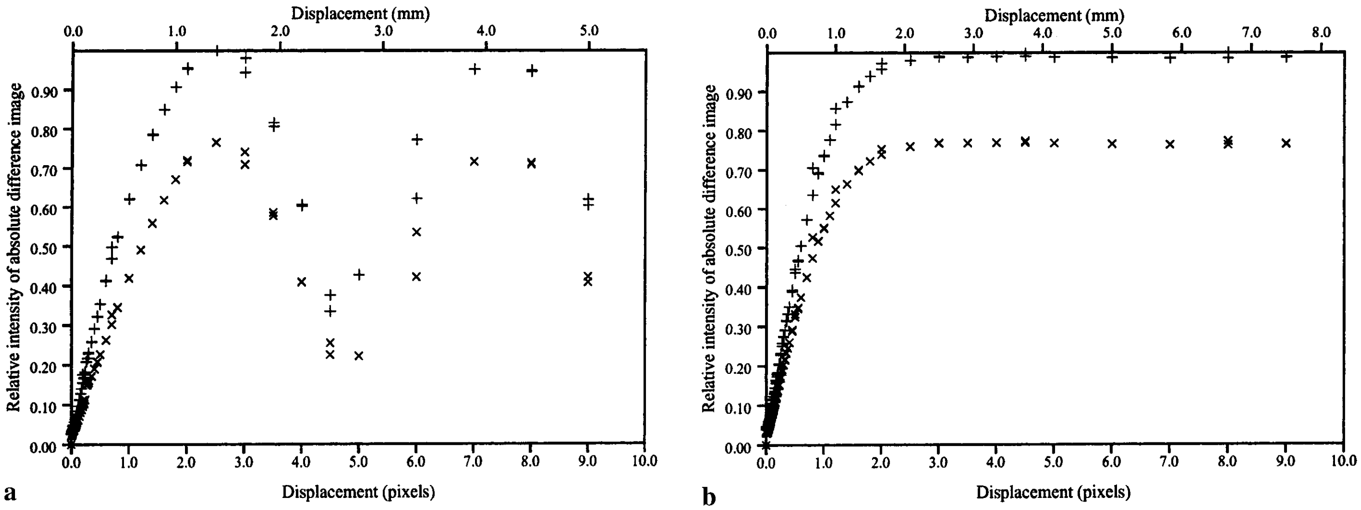

Fig. 8. Variations in the mean (+) and root mean square (×) value of $|P_{ij}(t) - P_{ij;0}|$ as the mask is displaced by a milling machine traverse for **a** a regular array of dots and **b** a random array of dots. The mask was traversed normal to the scan lines of the video camera for the regular array of dots, and parallel to the scan lines for the random array of dots

saturates at larger displacements. Tests have shown comparable results are obtained when traversing the dots parallel and normal to the scan lines of the video camera.

With a standard video camera the one-dimensional mask of the line-mode synthetic schlieren is less sensitive to signal noise than for the two-dimensional masks (i.e. dots) due to the fixed one-to-one relationship between rows of pixels on the CCD sensor and rows of pixels in the digitised image. If the mask is rotated by 90° so that the lines appear vertical we find the noise component is increased by a factor of two, reducing the measurable minimum displacement to approximately 0.02 pixels. The increased noise arises from the electronic jitter in the video signal and frame grabber which manifest themselves as random horizontal displacements of the image of the order of 0.04 pixels. This jitter was not noticeable when the lines were horizontal as the mask was approximately uniform in the direction of the jitter. The same issues arise when using the more complex dot mask geometries. The net result is that the maximum sensitivity may be achieved only when the lines on the mask are aligned closely with the scan lines of the video signal. We note, however, that if a digital camera and frame grabber were to be used, then this problem with signal jitter would be eliminated.

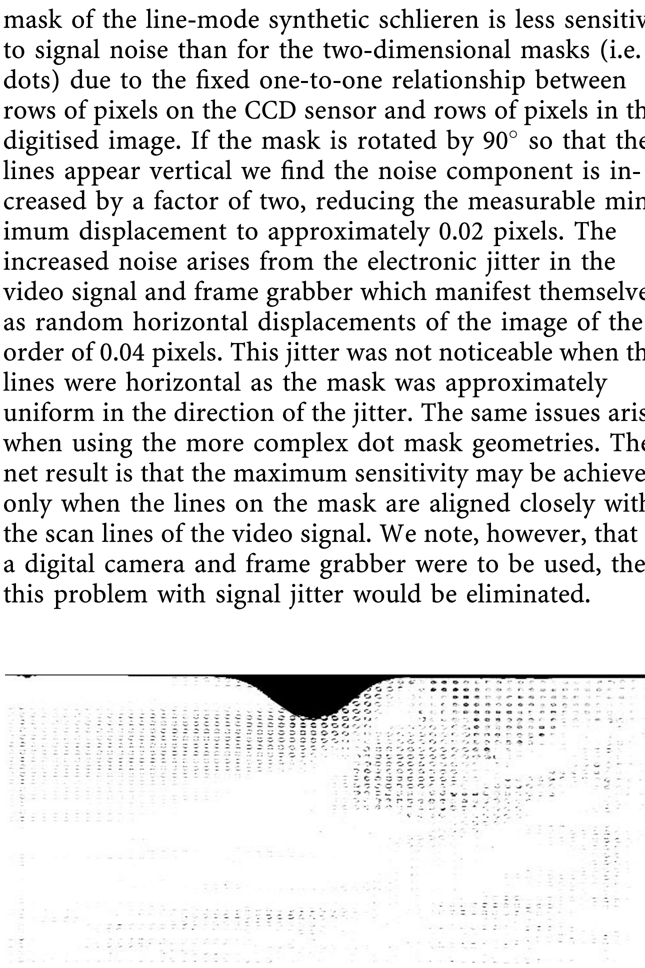

Fig. 9. Flow over a *hill* towed to the left through a linear salt stratification. The region of the tank visualised is approximately 2.5 m long and 1 m deep

Moreover, modern high resolution digital cameras will enable substantially higher sensitivities to be achieved.

One of the features of the synthetic schlieren techniques is the ability to scale it up to visualise flows at much larger scales than is feasible with conventional schlieren. For example, Fig. 9 shows the flow over a $h = 0.1$ m high 'hill' towed at a velocity $U = 0.055\,\mathrm{ms}^{-1}$ along a tank containing a nominally $N = 1.3\,\mathrm{s}^{-1}$ stratification, giving a Froude number $\mathrm{Fr} \equiv U/Nh \approx 0.4$. The field of view here is 1.3 m long and 0.6 m high. The ultimate size limit which may be visualised is given by the trade off between thermal noise and sensitivity, and the ability to produce a mask containing a suitable texture.

4.4
Preserving the sign

By preserving the sign information contained in $P_{ij}(t) - P_{ij;0}$ we can establish the direction of $\nabla\rho'$. Figure 10a is calculated from the same pair of images as Fig. 7a and c, but without taking the absolute value of the difference. Each crescent pair consists of one light crescent and one dark crescent. The gradient vector is directed from the darker toward the lighter crescent.

The simplicity of calculating $P_{ij}(t) - P_{ij;0}$, or some transformation of this, enables this qualitative measure of $\partial\rho'/\partial\uparrow$ or $\nabla\rho'$ to be determined in real-time using relatively simple hardware. Indeed the Data Translation DT2862 frame grabber card used for this work is a design ten years old yet allows calculation of $f(P_{ij}(t) - P_{ij;0})$ at full frame-rate video using a combination of an on-board arithmetic logic unit and on-board look-up tables. For the images presented in Figs. 5, 7 and 9 the look up table function was simply the calculation of the absolute value and the introduction of a scaling factor, while for Fig. 10a an offset is added instead.

A relatively simple extension of the above technique allows us to visualise the sign of the density gradients relatively easily for line mode. Whereas with the Moiré fringe method a $\pi/2$ phase shift between two sets of lines is

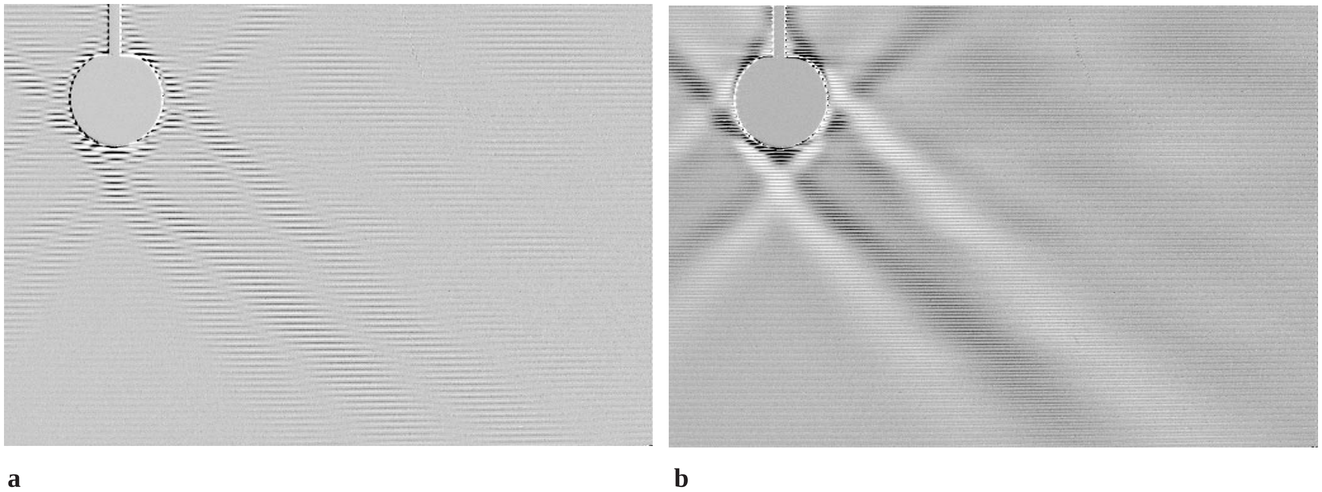

Fig. 10. Preserving the sign of the density gradient with qualitative synthetic schlieren. **a** As for figure 7a but without taking the absolute value of the difference. **b** As for figure 5a but calculating $\propto P_{ij;s}\,(P_{ij}(t) - P_{ij;0})$ with light regions representing positive $\partial\rho'/\partial z$ and dark regions negative $\partial\rho'/\partial z$

used, such phase shifting is not practical and unnecessary for synthetic schlieren. By utilising a line spacing greater than the "ideal" two pixels, we may construct

$$P_{ij;s} = \mathrm{sign}(\partial P_{ij;0}/\partial z) \quad , \tag{15}$$

and use this, where $|\partial p_{ij;0}/\partial z|$ is sufficiently large, to obtain the image

$$P_{ij;\partial} = P_{ij;s}(P_{ij}(t) - P_{ij;0}) \quad . \tag{16}$$

Figure 10b demonstrates the result of this additional processing on the images used for Fig. 5a to obtain the sign of the vertical gradient of the perturbation density. The image $P_{ij;\partial}$ is everywhere proportional to $\partial\rho'/\partial z$, but the constant of proportionality may vary spatially as the result of $p_0(x,y)$ taking values other than the 0 and 1 stated in (11). An obvious extension would be to factor out the illumination by normalising $P_{ij;0}$ and $P_{ij}(t)$ by the intensity of a mask containing no black lines. In the next section we shall introduce a more versatile approach to obtaining an accurate quantitative measure of $\nabla\rho'$ from the image pair $P_{ij;0}$ and $P_{ij}(t)$.

5
Line refractometry

To obtain quantitative information from the apparent motion of the lines on the mask we must introduce a more general model for the intensity reaching the CCD sensor in the video camera. The need for this model arises from an inability to form a sharp, uniform image of the mask on the CCD sensor. Typically the optics lead to some blurring, and the illumination of the mask is nonuniform, rendering the functional relationship between the images $P_{ij;0}$ and $P_{ij}(t)$, and the density gradient $\nabla\rho'$ more complex than suggested by (13). In this section we analyse the image formed by a mask of horizontal lines and show how quantitative information may be extracted.

Suppose the changes in the refractive index gradient give an apparent vertical displacement of the mask by some amount $\Delta\zeta$ at time t. We shall assume the curvature in ρ' is small so that $\Delta\zeta$ varies only over length scales large compared to the features contained in the mask.

As we have seen, the intensity of a pixel is related to the (unknown) intensity falling on the CCD sensor by (10). The combination of optical imperfections, noise and imperfections in the mask will ensure that $p(x,z;t)$ is a continuous function, even when the mask contains discrete steps. We may approximate $p(x,z;t)$ using a piecewise quadratic interpolation in a manner similar to that employed for numerical solution of the advection equation in control volume techniques. The idea here is that the approximation $P_{ij}(t) = p(x_i,z_j;t)$ (approximating the integral in (10) by the so-called mid-point rule for numerical integration) has an error $\mathrm{O}(\Delta z^3)$ which is of the same order as the error in a quadratic interpolation of the intensity (x_i,z_j). More specifically, if $\hat{P}_{0,ij}(z-z_j)$ is the quadratic interpolation of the unperturbed image around (x_i,z_j), we look to solve for the value $z - z_j = \Delta\zeta_{ij}$ such that $\hat{P}_{0,ij}(\Delta\zeta_{ij}) = P_{ij}(t)$. Thus the apparent displacement (in the z direction) of the mask $\Delta\zeta_{ij}$ is given by the roots of

$$\begin{aligned} &P_{0,0} - P + \tfrac{1}{2}(P_{0,1} - P_{0,-1})\Delta\zeta \\ &\quad + \tfrac{1}{2}(P_{0,1} - 2P_{0,0} + P_{0,-1})\Delta\zeta^2 = 0 \quad . \end{aligned} \tag{17}$$

Here we have used the shorthand $P = P_{ij}(t)$, $P_{0,0} = P_{0,ij}$, $P_{0,-1} = P_{0,i,j-1}$ and $P_{0,1} = P_{0,i,j+1}$. To avoid ambiguity as to which root of (17) should be taken, we solve (17) only if $P_{0,0}$ is intermediate between $P_{0,-1}$ and $P_{0,1}$, and the intensity contrast across the three lines is sufficiently large (i.e. $|P_{0,1} - P_{0,-1}| > \Delta P_{\min}$). Further, we select the root of (17) with smallest $|\Delta\zeta|$, effectively limiting $\Delta\zeta$ to be less than the spacing of the lines on the mask.

As an alternative to solving the quadratic expression for $\Delta\zeta$ given by (17), we may utilise a binomial expansion to show that his process has the same $\mathrm{O}(\Delta z^2)$ accuracy as assuming $\Delta\zeta$ is quadratic in $P_{0,ij}$. This latter approach was used by Sutherland et al. (1999) and gives

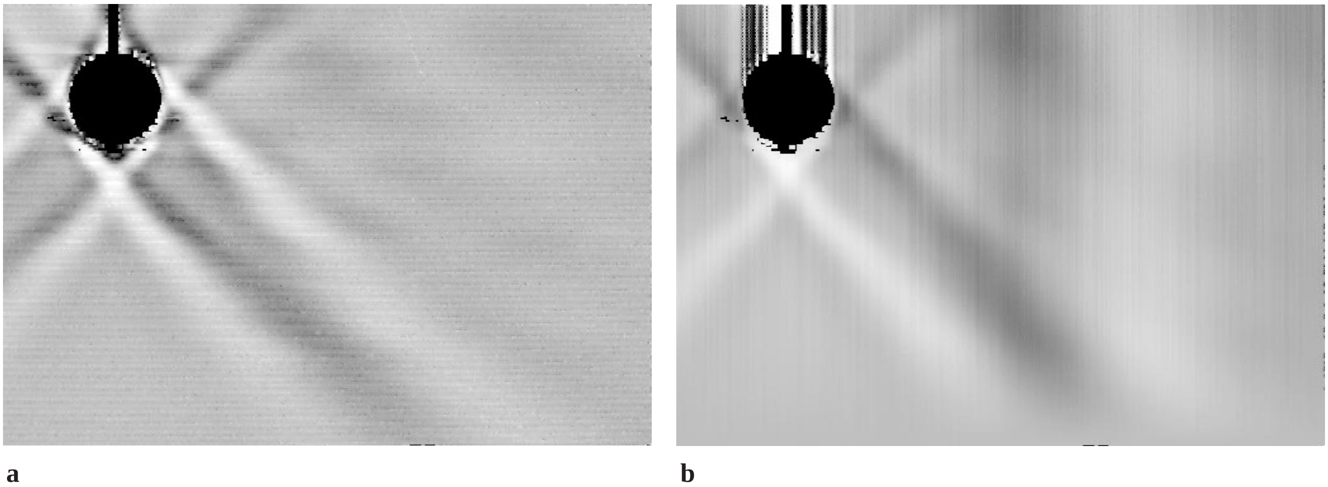

Fig. 11. Line mode refractometry for the internal wave field shown in Fig. 5a: **a** vertical perturbation density gradient $\partial\rho'/\partial z$ and **b** density perturbation ρ'

$$\Delta\zeta = \left[\frac{(P - P_{0,0})(P - P_{0,-1})}{(P_{0,1} - P_{0,0})(P_{0,1} - P_{0,-1})} - \frac{(P - P_{0,0})(P - P_{0,1})}{(P_{0,-1} - P_{0,0})(P_{0,-1} - P_{0,1})}\right]\Delta z \ . \qquad (18)$$

As with (17), $\Delta\zeta$ is calculated from (18) only if $P_{0,0}$ is intermediate between $P_{0,-1}$ and $P_{0,1}$, and there is sufficient intensity contrast across the three lines.

Once $\Delta\zeta$ has been determined from either (17) or (18), it is mapped from pixel space into physical space and (9) is applied to determine $\partial\rho'/\partial z$. Points for which Δz could not be calculated (typically points where $\partial P/\partial z$ is too small, as may occur if a line is centred on a pixel and would lead to an ambiguity in the sign of the displacement) are replaced by interpolated values using a Gaussian weighting function. The final result is scaled and used to construct an image representing $\partial\rho'/\partial z$ such as that shown in Fig. 11a for the same internal wave field as shown in Figs. 5a and 7. By assuming there is no density perturbation on the plane passing through the centre of the cylinder, this density gradient may be integrated with respect to z to obtain the density perturbation shown in Fig. 11b. We note, however, that wave reflections in this relative small tank ($605 \times 100 \times 400$ mm) generate density perturbations which extend throughout the domain and render the assumed 'boundary condition' inappropriate. The experiments of Sutherland et al. (1999), which were performed in a much larger tank, do not suffer the same problems with reflections and demonstrate the full power of this technique, providing more complete and accurate measurements of the internal wave field than was previously possible.

6
Dot tracking refractometry

With dot tracking refractometry, the mask consists of a regular array of dots. The precise position of each dot is determined using an intensity-weighted centroid relative to some local threshold (determined, for example, from the intensity histogram of a window larger than but approximately centred on the dot). The centroids of the dots are found first for the base flow, and then for each flow containing a density perturbation to be analysed. The difference in these two centroid locations $(\Delta\xi, \Delta\zeta)_{ij}$ for dot ij is related to the in-plane density gradient $\Delta\rho'_{ij}$ through (9). This two-dimensional density gradient field may then be integrated once, using an iterative method, to obtain the density perturbation field. The one arbitrary constant (the mean perturbation density) introduced by this process can normally be assumed to vanish.

The apparently simple procedure outlined above is made somewhat more complicated through the dots in the base and perturbed images not lying on a regular grid (although the mask is itself regular), and the possibility of the dots disappearing or being distorted to such an extent by $\nabla\rho'$ that ambiguities arise as to which dots are paired in the two images. Failure to consider these issues either gives rise to spurious displacement vectors (and hence errors in ρ') or limits the apparent displacements to be much less than the spacing between the dots.

The spatial resolution of the dot tracking refractometry is simply the spacing between the dots which, for a given CCD array, will necessarily be greater than the line spacing used for line refractometry as each dot must be resolved by at least two pixels in each direction. Sensitivity tests using the same set-up as described in Sect. 4.2, suggest that apparent displacements as small as 0.02 pixels can be measured for line refrectometry and 0.04 pixels for dot tracking refractometry. While the horizontal spatial resolution of dot tracking is substantially less than the pixel resolution achieved by line refractometry, dot tracking is able to recover both components of the density gradient and cope with larger apparent displacements of the mask. As a result it may be used in some situations where the line refractometry does not yield the required information.

Figure 12a shows ρ' calculated from dot tracking refractometry for the same internal wave field used for Fig. 7a. The density perturbation calculated from dot

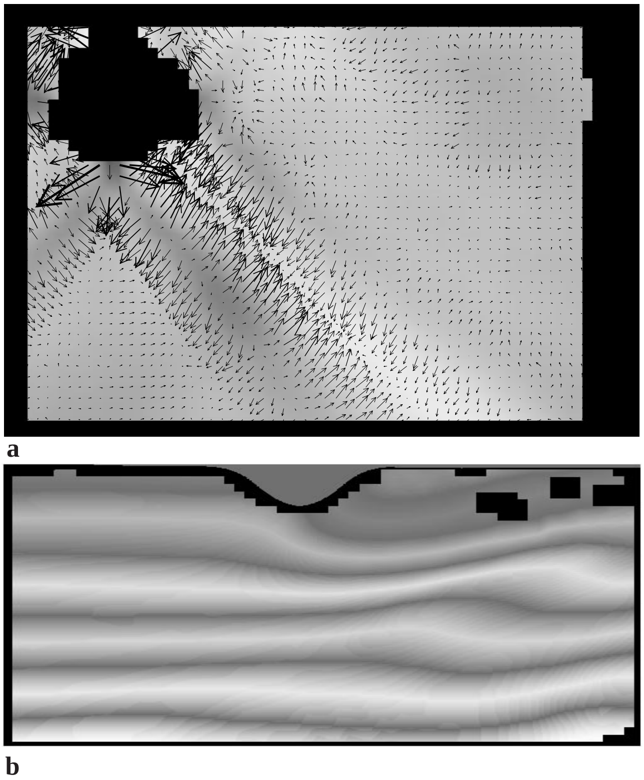

Fig. 12. Dot tracking refractometry. **a** Perturbation density ρ' (greyscale) and gradient $\nabla\rho'$ (arrows) for oscillating cylinder internal wave field in Fig. 7a. **b** Complete density field (showing contours of constant density) for flow over a towed hill shown in Fig. 9

tracking refractometry is somewhat smoother than line refractometry because a knowledge of $\partial\rho'/\partial x$ removes the accumulation of errors associated with the uncoupled vertical integrations used for the latter. The superimposed arrows represent the gradient in the perturbation density $\nabla\rho'$ and illustrate the size and direction of the apparent movement of the mask. Figure 12b shows the complete density field for the waves over the towed hill presented qualitatively in Fig. 9.

The dot tracking method may also be used in conjunction with lines with only minor modifications to the algorithm. The results are similar to those obtained with the interpolation method presented in the previous section. The main limiting feature of both dot tracking and line interpolation is the trade off between a limited dynamic range and spatial resolution. In both cases the maximum useable apparent displacement is comparable with the dot or line spacing. Larger apparent displacements lead to ambiguities. At the same time the spatial resolution is limited to the spacing of the dots or lines. Hence increasing the dynamic range leads to a reduced spatial resolution. In many circumstances it is possible to achieve a dynamic range of O(100:1) between the largest and smallest values of $\Delta\rho'$ while retaining an adequate spatial resolution. In other flows higher spatial resolutions may be required without compromising the dynamic range and the next section outlines an alternate to extracting the apparent motion of the mask which offers an improved balance between these two considerations.

7

Pattern matching refractometry

The final variant we consider here draws on the same ideas as employed for particle image velocimetry (PIV; a more appropriate name would be pattern matching velocimetry or PMV). For the results presented in this paper the mask consists of a randomised array of dots (as used for Fig. 7b) so that each window large enough to cover several dots will contain a unique pattern of dots. The only requirement for the mask, however, is that it has a strong texture which does not repeat itself except over length scales large compared with the apparent movement of the mask. Ideally it should have high contrast and the individual features of a size just detectable by the video camera used.

As with the techniques outlined in the previous sections, the refractive index perturbations associated with ρ' will then appear to shift the texture of the mask. Provided the curvature terms $\partial^2\rho'/\partial x^2$ and $\partial^2\rho'/\partial z^2$ do not lead to large distortions of the patterns, establishing the apparent displacement field is simply a matter of determining the shift that has to be applied to a window containing a subregion of the textured image to map it back on to the image of the unperturbed flow.

This process is somewhat cleaner than the comparable PIV problem as we can control the uniformity of the "particle seeding", and we do not have to worry about three-dimensional effects causing particles to enter or leave the "light sheet". Dots, or whatever texture is used for the mask, can still disappear if the curvature in the density perturbation is too large, but this does not represent a difficulty in practice except in so far as the gradients will not be resolved adequately in such regions.

As with PIV, a variety of pattern matching algorithms are possible. Indeed our first tests of this method utilised simple PIV routines written in 1991 based on optimising one of three objective functions:

$$f_{\mathrm{cross}}(\Delta\xi,\Delta\zeta;x_i,z_j) = -\frac{\langle P(x+\Delta\xi,z+\Delta\zeta;t)P_0(x,z)\rangle - \langle P(x+\Delta\xi,z+\Delta\zeta;t)\rangle\langle P_0(x,z)\rangle}{\left[\langle P(x+\Delta\xi,z+\Delta\zeta;t)^2\rangle - \langle P(x+\Delta\xi,z+\Delta\zeta;t)\rangle^2\right]^{1/2}\left[\langle P_0(x+z)^2\rangle - \langle P_0(x,z)\rangle^2\right]^{1/2}} \tag{19}$$

$$f_{\mathrm{abs}}(\Delta\xi,\Delta\zeta;x_i,z_j) = \langle|P(x+\Delta\xi,z+\Delta\zeta;t) - P_0(x,z)|\rangle \ , \tag{20}$$

$$f_{\mathrm{sq}}(\Delta\xi,\Delta\zeta;x_i,z_j) = \langle[P(x+\Delta\xi,z+\Delta\zeta;t) - P_0(x,z)]^2\rangle \ . \tag{21}$$

In each of these $\langle\varphi(x,z)\rangle$ represents the average of φ calculated over all pixels falling in the interrogation window described by $x_i - w_x \le x \le x_i + w_x$ and $z_j - w_z \le z \le z_j + w_z$, where $x_i,\ z_j$ describes the location

Table 1. Displacements (in mm) calculated using different matching algorithms

Description	Simple		Interpolate three times	
Nominal displacement from digital readout	0.100 ± 0.010	1.000 ± 0.010	0.100 ± 0.010	1.000 ± 0.010
f_{cross}, biquadratic fit	0.066 ± 0.017	0.975 ± 0.020	0.086 ± 0.012	1.011 ± 0.018
f_{abs}, biquadratic fit	0.051 ± 0.014	0.939 ± 0.019	0.072 ± 0.011	0.972 ± 0.018
f_{sq}, biquadratic fit	0.067 ± 0.015	0.975 ± 0.020	0.071 ± 0.011	0.989 ± 0.018
Average	0.061 ± 0.015	0.963 ± 0.020	0.076 ± 0.011	0.991 ± 0.018

of the centre of the window of width $2w_x$ and height $2w_z$. The f_{cross} objective function is that typically used by most investigators for PIV (note that here the cross correlation function is evaluated directly rather than imposing a periodicity constraint and using Fast Fourier Transforms). The f_{abs} and f_{sq} objective functions are computationally simpler (and were originally introduced as they could be calculated by the frame hardware an order or magnitude faster than the CPU could process the images) and therefore faster to compute. In all cases the objective function is minimised (hence the negative sign in (19)), although there are a number of algorithms for doing so. In this paper we consider two such algorithms.

The first algorithm minimises the objective function for integer values of $\Delta\xi$ and $\Delta\zeta$ to obtain a pixel-resolution measure of the apparent displacement. A surface (biquadratic in this case) is then fitted in the neighbourhood of this minimum to provide subpixel resolution for the optimal shift. The performance of the pattern matching refractometry using this algorithm, and the relative merits of f_{cross}, f_{abs} and f_{sq}, have been assessed by a sensitivity study similar to that in Sect. 4.2. The results of this study are presented in Table 1 in the column headed “Simple”. The values quoted are the mean and standard deviation of the displacements calculated using interrogation windows 15×15 pixels at 625 separate locations. The same pair of images was used for each objective function for a given traverse displacement.

The second algorithm is similar to the first but rather than restricting the calculation of f_{cross}, f_{abs} or f_{sq} to integer values of $(\Delta\xi,\ \Delta\zeta)$, we interpolate the image to obtain values for $P(x + \Delta\xi, z + \Delta\zeta; t)$ (for use in (19), (20) or (21)) with noninteger $(\Delta\xi, \Delta\zeta)(<1)$ in the neighbourhood of the minimum identified by the biquadratic fit. The objective functions f_{cross}, f_{abs} or f_{sq} are calculated from the interpolated image and a biquadratic function is again fitted in the neighbourhood of the minimum to obtain the optimal $(\Delta\xi, \Delta\zeta)$. This process can be repeated (with $P(x + \Delta\xi,\ z + \Delta\zeta; t)$ calculated over decreasing intervals) if so desired. For the results presented in Table 1 the image interpolation was restricted to be bilinear. To improve the computational efficiency of this process, multigrid methods are employed whereby for successive outer iterations the spatial resolution is doubled and the search region for the pattern matching is reduced.

Comparison of the results presented in Table 1 using the two competing algorithms and three different objective functions suggests some improvement may be gained by using the interpolating algorithm with a reduction in the standard deviation of the displacements calculated for a

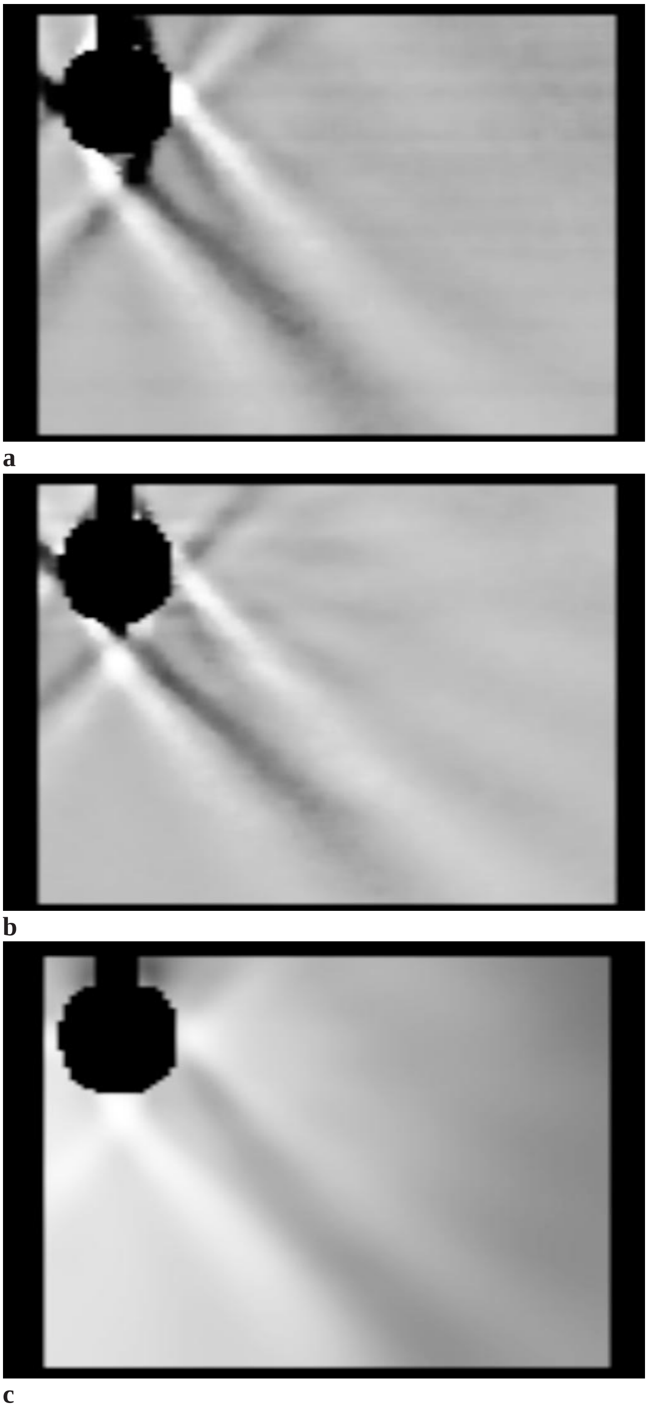

Fig. 13. Pattern matching refractometry. **a** Horizontal gradient $\partial\rho'/\partial z$, **b** vertical gradient $\partial\rho'/\partial z$, and **c** perturbation density ρ' for oscillating cylinder internal wave field shown in Fig. 7b

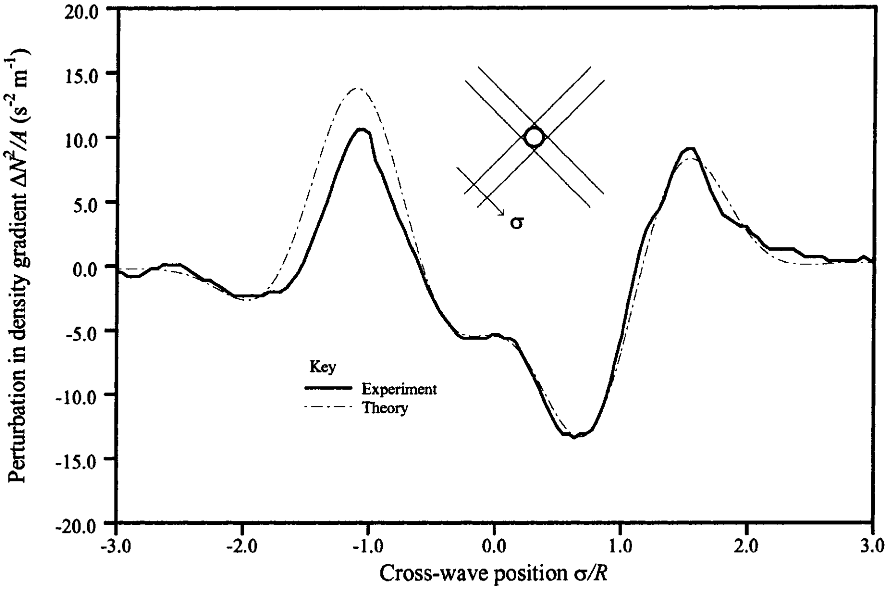

Fig. 14. Comparison between experiment (solid line) theory (dashed line) for the cross-beam structure of the vertical gradient in the perturbation density a distance $8R$ from the cylinder. The cross-beam coordinate σ is centred on the wave beam with the orientation shown in the insert

given image pair and a slight convergence of the different objective functions. The difference between the three objective functions with the interpolating algorithm allows us to estimate an upper bound for the error associated with the algorithm/objective function combination as approximately 0.01 mm ($\sim$0.01 pixels). The standard deviations for each algorithm, function and displacement are approximately constant and somewhat less than 0.02 mm (0.02 pixels). We believe this standard deviation represents the optical distortion, thermal and signal noise in the pair of images. The final component of the difference between the displacement from the digital readout, and that calculated by the pattern matching is due to mechanical imperfections in the traverse and digital readout and is consistent with the $\pm$0.010 mm quoted by the manufacturer.

Figure 13 illustrates the performance of pattern matching refractometry (using an 11×11 pixel interrogation window) with the same flow as used for previous methods. Figure 13a and b show the two components of the gradient of the density perturbation, while Fig. 13c shows the density perturbation itself. Note that, as with the earlier density fields, reflections from the boundaries of the tank make this wave field much more complex than expected and remove some of the normal symmetries.

Figure 14 compares the experimentally measured gradient in the perturbation density field with viscous theory. The solid curve shows the experimental measurement obtained by pattern matching refractometry along a line normal to the lower left beam of the internal waves with $\omega/N = 2^{-1/2}$ at a distance of 8 radii from the cylinder as the cylinder reaches the bottom of its stroke. The dashed curve is the prediction from the theory of Hurley and Keady (1997) for the same conditions. The systematic differences are here dominated by reflections of the internal waves from the tank boundaries. A similar level of agreement is found at other phases of oscillation. Sutherland et al. (1999) have presented a more detailed comparison and analysis of this flow using line refractometry and found some systematic differences related to the boundary layer approximations used in Hurley and Keady's theory.

When compared with the dot tracking refractometry in Sect. 6 the advantages of pattern matching refractometry are the ability to operate at higher spatial resolutions and with larger apparent displacements of the mask. The spatial resolution for pattern matching refractometry is again controlled by the dot spacing, but here the dots will typically be smaller and closer together. The use of overlapping pattern windows optimises the resolution. The larger the windows the greater the resolution in $\nabla\rho'$, but the lower the spatial resolution. In dot tracking refractometry the maximum apparent displacements were limited by the dot spacing as larger movements lead to aliasing errors. With pattern matching refractometry the patterns can have substantial apparent displacements as each region of the pattern retains its own unique identity. On the down side the computational cost per displacement vector is substantially larger, but with the ever-increasing performance of computer hardware, this is unlikely to represent a serious issue.

8
Conclusions

The synthetic schlieren techniques outlined in this paper are able to provide qualitative visualisations of a sensitivity and nature comparable with classical schlieren, yet are substantially easier to set up and may be scaled to cope with flows in significantly larger domains without expensive parabolic mirrors. Obtaining quantitative measurements of the density perturbation is a relatively simple extension, with a number of distinct methods of obtaining the required information being described. It is unfortunate that the set-up for the experiments used here to illustrate the techniques resulted in the visualisations being contaminated by reflected waves, and that there was a high level of thermal noise in the laboratory significantly reducing the signal to noise ratio.

Perhaps the biggest drawback compared with traditional schlieren is the reduced spatial resolution. For many flows, such as the internal waves used here to illustrate the methods, this is unimportant as the curvature in the density field remains small. In some cases, however, it is important to resolve both the regions of high curvature, where the apparent displacement of light rays may occur over scales comparable to or smaller than the spacing of the mask elements, and regions of low curvature in ρ'. We are currently investigating a hybrid of shadowgraphy and the synthetic schlieren techniques reported here by which simultaneous measurements of $\nabla^2\rho'$ and $\nabla\rho'$ could be made to improve the resolution of fronts, shocks or layers.

While quantitative information requires the flow to be two-dimensional, useful measurements and qualitative visualisations may also be obtained in weakly three-dimensional and turbulent flows, as illustrated by the image of thermal convection from a hand shown in Fig. 5b. The methods described here may also be used to obtain measurements of depth or layer depth when a free surface or internal interface are present, provided the refractive indices are constant within the layer (or layers). Further discussion on these alternative applications is beyond the scope of this paper.

Each of the three quantitative techniques reported here has its strengths. We believe, however, that ultimately pattern matching refractometry will prove to be the most useful and versatile. It is the easiest to set up as its does not require alignment of the mask and video system, and the precise form of the mask is unimportant. Moreover, it offers the measurement of both components of $\nabla\rho'$ while achieving both a large dynamic range and good spatial resolution.

References

Burton RA (1949) A modified schlieren apparatus for large areas of field. J Opt Soc Amer 39: 907–909

Dalziel SB; Hughes GO; Sutherland BR (1998) Synthetic schlieren. In: Carlomagno; Grant (ed) Proceedings of the 8th International Symposium on Flow Visualization, ISBN 0 9533991 0 9, paper 062

Gill AE (1982) Atmosphere-Ocean Dynamics, Academic Press, London, 662 pp

Greenberg PS; Klimek RB; Buchele DR (1995) Quantitative rainbow schlieren deflectometry. Appl Optics 34: 3810–3822

Hurley DG; Keady G (1997) The generation of internal waves by vibrating cylinders, Part 2: Approximate viscous solution for a circular cylinder. J Fluid Mech 351: 119–138

Irvin BR; Ross J (1991) Observations of pattern evolution in thermal convection with high-resolution quantitative schlieren imaging. Phys Fluids A 3: 1699–1710

Lin J-C; Rockwell D (1997) Quantitative interpretation of vortices from a cylinder oscillating in quiescent fluid. Expts in Fluids 23: 99–104

Merzkirch W; Peters F (1992) Optical visualisation of internal gravity waves in stratified fluid. Optics and Lasers in Engineering Vol. 16 pp. 411–425

Mortensen TA (1950) An improved schlieren apparatus employing multiple slit-gratings. Rev Sci Instrum 21: 3–6

Mowbray DE; Rarity BSH (1967) A theoretical and experimental investigation of the phase configuration of internal waves of small amplitude in a density stratified liquid. J Fluid Mech 28: 1–16

Peters F (1985) Schlieren interferometry applied to a gravity wave in a density-stratified liquid. Expts in Fluids 3: 261–269

Sakai S (1990) Visualisation of internal gravity waves by Moiré method. Kashika-Joho 10: 65–68

Sutherland BR; Dalziel SB; Hughes GO; Linden PF (1999) Visualisation and measurement of internal waves by "synthetic schlieren". Part I: Vertically oscillating cylinder; to J Fluid Mech 390: 93–126

Turner JS (1973) Buoyancy effects in fluids, Cambridge University Press, 368 pp

Weast RC (1981) Handbook of chemistry and physics C.R.C. Press, 62 edition

Weyl FJ (1954) Analysis of optical methods. In Ladenburg RW (ed) Physical measurements in gas dynamics and combustion. Princeton University Press, Princeton, New Jersey, 3–25

van Dyke M (1982) An album of fluid motion, Parabolic press, Stanford, 176 pp